Blowout regimes of plasma wakefield acceleration

K. V. Lotov
Budker Institute of Nuclear Physics, 630090, Novosibirsk, Russia
and Novosibirsk State University, 630090, Novosibirsk, Russia
(Received 8 October 2003; published 27 April 2004)

A wide region of beam parameters is numerically scanned and the dependence of wakefield properties on the beam length and current is clarified for the blowout regime of beam-plasma interaction. The main regimes of the plasma response are found, which qualitatively differ in the plasma behavior. To characterize the efficiency of the energy exchange between the beam and the plasma, the energy flux through the comoving window is introduced. Scalings of the energy flux for the linear plasma response and the main blowout regimes are studied. The most efficient energy transfer occurs in the so-called "strong beam" regime of interaction. For this regime, analytical approximations for various aspects of the plasma response are obtained.

DOI: 10.1103/PhysRevE.69.046405 PACS number(s): 52.40.Mj, 41.75.Lx, 52.35.Mw

I. INTRODUCTION

This paper is related to electron-beam-driven acceleration of particles in plasmas [1] (termed plasma wakefield acceleration, PWFA). PWFA is of great interest due to availability of high accelerating gradients (orders of magnitude higher than those in conventional accelerators) and intrinsically long acceleration distance that is not limited by driver diffraction or dephasing (unlike laser-driven wakefield schemes). Reviews of PWFA basics can be found in Refs. [2–4].

Several PWFA schemes were proposed that differ in the drive beam configuration [1,5–8]. Here we study the so-called blowout regime in which the head of a short driver ejects all the plasma electrons from its propagation channel and most part of the beam propagates in the electron-free region (termed the cavern henceforth). The blowout regime has been extensively studied both theoretically [8–15] and experimentally [3,16–22].

Most of the recent theoretical studies of the blowout PWFA were concentrated on the beam and plasma parameters of SLAC E-157 experiment [11–15]. However, the optimum regimes of the wakefield accelerator may not fall into parameter regions accessible with today's facilities. In this paper we scan a much wider parameter area and study the plasma response to a dense drive beam for various beam sizes and currents. We also introduce the total energy flux as a measure of beam-plasma energy exchange and study its scalings.

The paper is organized as follows. In Sec. II we describe the mathematical model adopted for the beam and plasma and the code used for simulations. In Sec. III we present the map of blowout PWFA regimes and describe the main asymptotic cases. In Sec. IV we derive an analytical approximate formula for various cavern parameters in the special case of a "strong beam." In Sec. V we show the main scalings for geometrical parameters of the cavern and describe the motion of plasma electrons in various regimes. In Sec. VI we introduce the total energy flux and study its scalings in the linear and blowout regimes of PWFA. The main results of the paper are emphasized in the Summary.

II. THE MODEL AND THE CODE

We consider a dense axisymmetric ultrarelativistic electron beam propagating through the infinite fully ionized cold plasma of a constant density n_0 (Fig. 1). Our aim is to study the plasma response to beams of various length, radius, and peak current. The long-term beam dynamics, a role of the plasma temperature or inhomogeneity, and the plasma response to beams of exotic shapes are beyond the scope of this paper. We also neglect the motion of plasma ions since, in the time of interest, the ions cannot shift considerably. There is no external magnetic field in the system.

Since the time scale of beam evolution is much longer than the plasma time scale, the problems of beam dynamics and plasma response get decoupled, and we can consider the beam as a "rigid" nonevolving charge distribution propagating with the velocity of light c. Correspondingly, the picture of plasma fields and currents does not change in the window that moves with the beam.

In the comoving window we use the cylindric coordinates (r,φ,ξ), where ξ is related to the laboratory coordinate z and time t as $\xi=z-ct$. The beam density is taken in the form

$$n_b(r,\xi)=\frac{I_{b,max}}{4\pi ec\sigma_r^2}e^{-r^2/2\sigma_r^2}\left[1+\cos\left(\frac{\xi}{\sigma_z}\sqrt{\frac{\pi}{2}}\right)\right],\quad |\xi|<\sigma_z\sqrt{2\pi}, \tag{1}$$

where $I_{b,max}$ is the peak beam current, σ_r and σ_z are the beam dimensions, and $e>0$ is the elementary charge. This cosine distribution over ξ is more convenient for simulations than the Gaussian one because it smoothly vanishes outside an

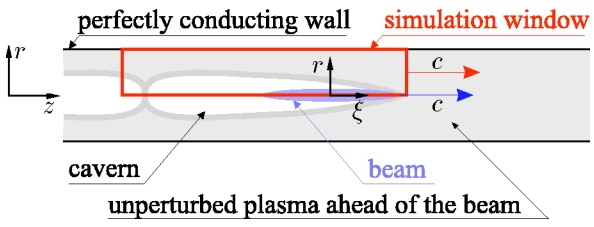

FIG. 1. (Color online) Geometry of the problem.

interval of finite length. It is close to the distribution

$$n_b(r,\xi) = \frac{I_{b,max}}{2\pi ec\sigma_r^2}\exp\left(-\frac{r^2}{2\sigma_r^2}-\frac{\xi^2}{2\sigma_z^2}\right) \tag{2}$$

and contains the same number of particles.

For calculation of the plasma response, we use the code LCODE [15,23]. In simulations, plasma electrons are modeled by macroparticles, while plasma ions are the immobile background charge. Each macroparticle is characterized by six quantities: the transverse coordinate r, three components of the momentum (p_r, p_φ, and p_z), mass M, and charge q. The longitudinal coordinate ξ is not a parameter here, but an argument. Since the beam is rigid, all particles starting from a given radius copy the motion of each other, and their parameters (r, p_r, p_φ, and p_z) can be found as functions of ξ.

Parameters of plasma macroparticles are initialized ahead of the beam (at $\xi=\sigma_z\sqrt{2\pi}$) and then calculated layer by layer according to the equations

$$\frac{d\vec{p}}{d\xi} = \frac{d\vec{p}}{dt}\frac{dt}{d\xi} = \frac{q}{v_z - c}\left(\vec{E} + \frac{1}{c}[\vec{v}\times\vec{B}]\right), \tag{3}$$

$$\frac{dr}{d\xi} = \frac{v_r}{v_z - c}, \quad \vec{v} = \frac{\vec{p}}{\sqrt{M^2 + p^2/c^2}}. \tag{4}$$

The plasma current and electron density are obtained by summation over the macroparticles lying within a given radial interval:

$$\vec{j} = A\sum_i \frac{q_i\vec{v}_i}{c - v_{z,i}}, \quad n = -A\sum_i \frac{q_i/e}{c - v_{z,i}}, \tag{5}$$

where A is a normalization factor. The denominator in Eq. (5) appears since contributions of a macroparticle to the density and current depend on the macroparticle speed in the simulation window. This plasma model is similar to that used in Ref. [24] for fast simulations of laser-plasma interactions.

Knowing $\vec{j}$ and n at some ξ, we obtain the fields in the corresponding layer from the Maxwell equations that, under the condition

$$\partial/\partial\xi = \partial/\partial z = -\partial/\partial(ct), \tag{6}$$

are reduced to the equations

$$\frac{1}{r}\frac{\partial}{\partial r}rE_r = -4\pi e(n + n_b - n_0) - \frac{\partial E_z}{\partial\xi}, \tag{7}$$

$$\frac{\partial(E_r - B_\varphi)}{\partial\xi} = \frac{\partial E_z}{\partial r} = \frac{4\pi}{c}j_r. \tag{8}$$

The plasma response is calculated layer by layer towards the decreasing ξ (from right to left in Fig. 1). Both r and ξ steps are $0.005\ c/\omega_p$, where $\omega_p=\sqrt{4\pi n_0 e^2/m}$ is the unperturbed plasma frequency. The ξ step is automatically decreased near field singularities [15]. Typically, ten macroparticles per r step are used.

Deriving various scalings, we use dimensionless quantities and denote them by tildes, for example,

$$\tilde{I}_m = \frac{eI_{b,max}}{mc^3}, \quad \tilde{\sigma}_z = \frac{\sigma_z\omega_p}{c}, \quad \tilde{n} = \frac{n}{n_0}, \quad \tilde{E}_z = \frac{E_z}{E_0}, \tag{9}$$

where $E_0=\sqrt{4\pi n_0 mc^2}$.

III. MAP OF BLOWOUT REGIMES

There are three parameters in our model which determine the plasma response: $I_{b,max}$, σ_z, and σ_r. For beams of a small radius ($\sigma_r \ll c/\omega_p$), the plasma response weakly depends on σ_r, so we can plot a two-dimensional map of cavern regimes on the plane ($\sigma_z, I_{b,max}$) [Fig. 2(a)]. The case $\sigma_r \gtrsim c/\omega_p$ is less interesting since wide beams always produce a weaker wakefield than narrow beams of the same current.

All simulations presented in the paper are made for $\sigma_r = 0.1\ c/\omega_p$ unless stated otherwise. The map is deliberately extended to the region of high beam currents. These currents can be obtained by longitudinal compression of a high-energy beam and should also be analyzed.

For long beams, we observe the regime at which the beam smoothly moves plasma electrons aside and leaves no much perturbations behind [Fig. 2(c)]. In this regime, the longitudinal electric field is rather small; it decelerates the front half of the beam and accelerates the tail half. The cavern is long; it is usually termed "ion channel." The channel has its maximum width at the place of maximum beam current. Dimensions of the channel, electromagnetic fields in the system, plasma current, and density are in a good agreement with the infinite beam model [25–28]. According to the model, the plasma response to the beam is local, i.e., it is completely determined by the beam current at this cross section. The theoretically predicted channel radius is shown in Fig. 2(c) by the "theory" line. The beam in the ion channel regime is subject to the instability of two-stream nature, when a transverse shift of the beam couples with a disturbance of the channel boundary [29–31].

As the beam shortens or the beam current increases, there appear strong oscillations of the cavern boundary [Fig. 2(e)] which continue after the beam passage. Most part of the beam energy remains in the plasma, and field oscillations take a singular form. The widest place of the cavern shifts behind the cross section of maximum beam current, and the cavern itself gets wider than predicted by the infinite beam model (theory line). In Fig. 2(a) we show several lines that quantitatively characterize these changes (from bottom right to top left): the line where 95% of the energy taken from the decelerated beam head is recuperated by the accelerated beam tail, the line showing $0.5\sigma_z$ lag of the widest cavern place behind the beam center, the line where the cavern is 20% wider than predicted by the infinite beam model, the line showing 5% of energy recuperation by the accelerated tail of the beam, and the line where the cavern radius has its maximum as a function of σ_z.

At high beam currents and moderate beam lengths, we observe the "strong beam" regime of the blowout [Fig. 2(g)]. In this regime, most part of the beam sees high-amplitude

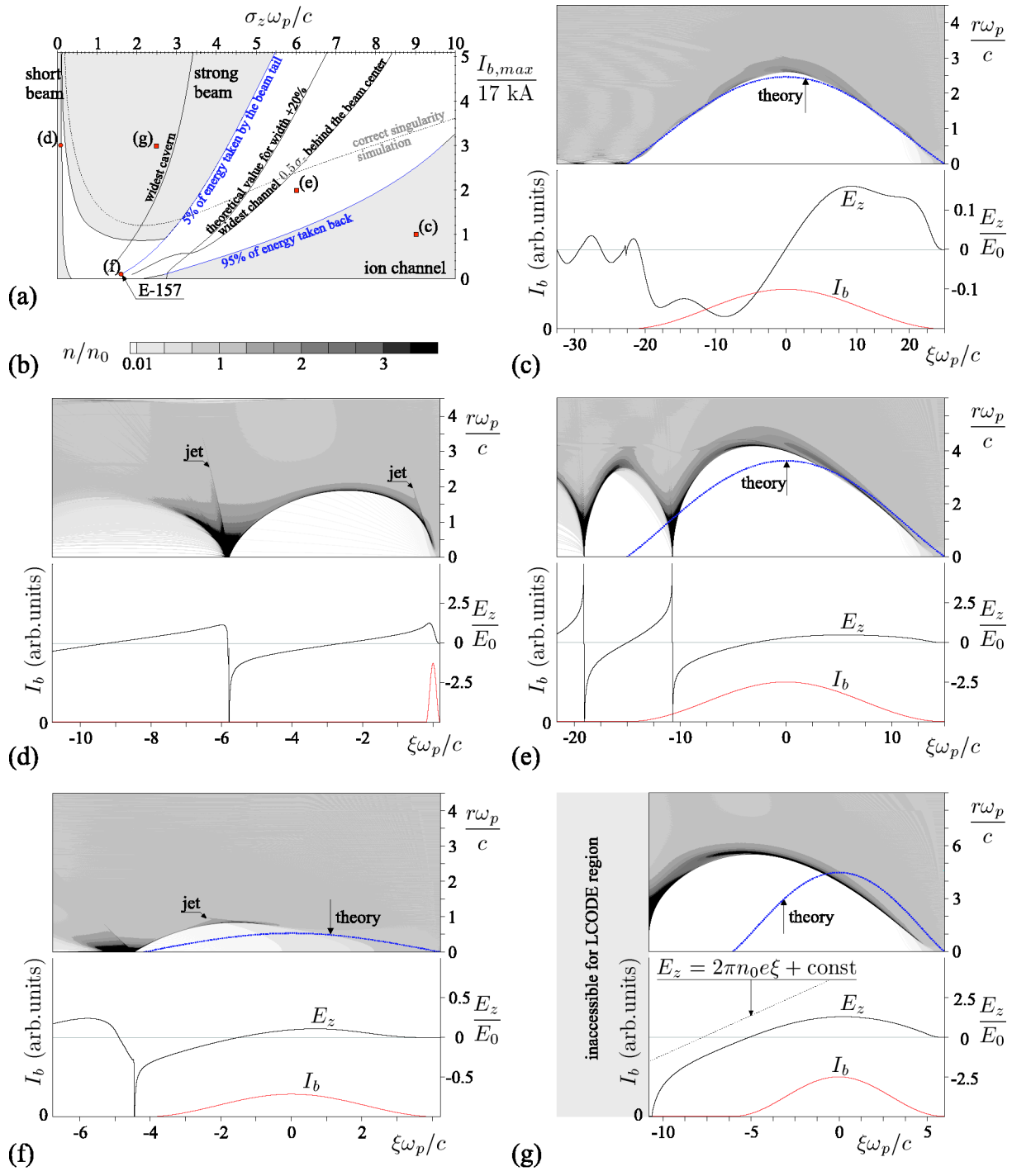

FIG. 2. (Color online) The map of blowout regimes (a), the palette used for electron density maps (b), the plasma electron density (grayscale maps), longitudinal on-axis electric field E_z, and beam current I_b for various regimes: ion channel (c), short beam (d), perturbed ion channel (e), E-157 beam (f), and strong beam (g).

decelerating field and efficiently transfers the energy to the plasma. The cavern is essentially asymmetric, its widest place is located near the beam end, and the cavern itself is noticeably longer and wider than predicted by the theory (theory line). A narrow high-density electron layer is formed near the cavern boundary (screening layer) so that perturbations do not deeply penetrate into the plasma.

In the strong beam regime, some plasma electrons get captured by the large electric field at the end of the cavern and get accelerated up to hundreds of MeV. This phenomenon cannot be self-consistently modeled within the adopted plasma model and causes a code fault. Thus, for sufficiently strong beams this code can simulate only the first period of the wakefield up to the singularity. The area of correct simulation beyond the singularity is located in Fig. 2(a) below the gray line.

For short beams, we observe the third main regime of the blowout [Fig. 2(d)]. In this regime, the beam acts similar to

the point charge. Nearby electrons receive an instant push and form a clearly visible diverging jet. Far electrons form the screening layer (not as dense as for strong beams) and define a tear-shaped form of the cavern (which is wider at the front half). Near the singularity, the second jet of plasma electrons is formed. The field singularity itself is asymmetric.

The transitions between the main regimes are smooth, so the definition of regime boundaries is somewhat arbitrary. To draw several boundaries in Fig. 2(a), we use the energy flux described in Sec. VI. In the "short beam" area, the scaling (77) is correct up to 20%. In the "strong beam" area, the dimensionless energy flux (69) behind the beam is $\tilde{\Psi} > 20$.

The regime of E-157 experiment [11–15] is shown in Fig. 2(f). It is located at the transition between the main cavern regimes and contains a mixture of the above-discussed features. As for long beams, the dimensions of the cavern are close to theoretical values. As for strong beams, most part of the beam is decelerated. As for short beams, we observe the jet of scattered electrons and asymmetric field singularity.

IV. ANALYTICS FOR STRONG BEAMS

Before describing specific properties of the strong beam regime, we recall some general features of the blowout PWFA. In the absence of plasma electrons ($j_r \equiv 0, n \equiv 0$), it directly follows from Eq. (8) that the longitudinal electric field is constant across the cavern:

$$\frac{\partial E_z}{\partial r} = 0. \tag{10}$$

From the Poisson and Maxwell equations

$$\frac{1}{r}\frac{\partial}{\partial r} r E_r = 4\pi e(n_0 - n_b) - \frac{\partial E_z}{\partial \xi}, \tag{11}$$

$$\frac{1}{r}\frac{\partial}{\partial r} r B_\varphi = -4\pi e n_b - \frac{\partial E_z}{\partial \xi}, \tag{12}$$

we find that the focusing force on the ultrarelativistic beam is linear inside the cavern:

$$F_r = -e(E_r - B_\varphi) = -2\pi n_0 e^2 r. \tag{13}$$

An analytical treatment of the strong beam case is possible owing to the narrow screening layer that separates the cavern and surrounding unperturbed plasma. The electrons in this layer move coherently with nearly equal velocities. The ξ dependencies of layer velocity components are shown in Fig. 3(a) [all illustrations in this section are made for $I_{b,max} = 51$ kA, $\sigma_z = 2.4\, c/\omega_p$, Fig. 2(g)].

We can introduce the surface density of the screening layer

$$\Lambda = \int_{\text{layer}} n\, dr, \tag{14}$$

e.g., by integration over $n > 2n_0$ region (the result is insensitive to the layer detection threshold). As follows from Eq. (8), this quantity approximately relates E_z inside the cavern with the layer velocity:

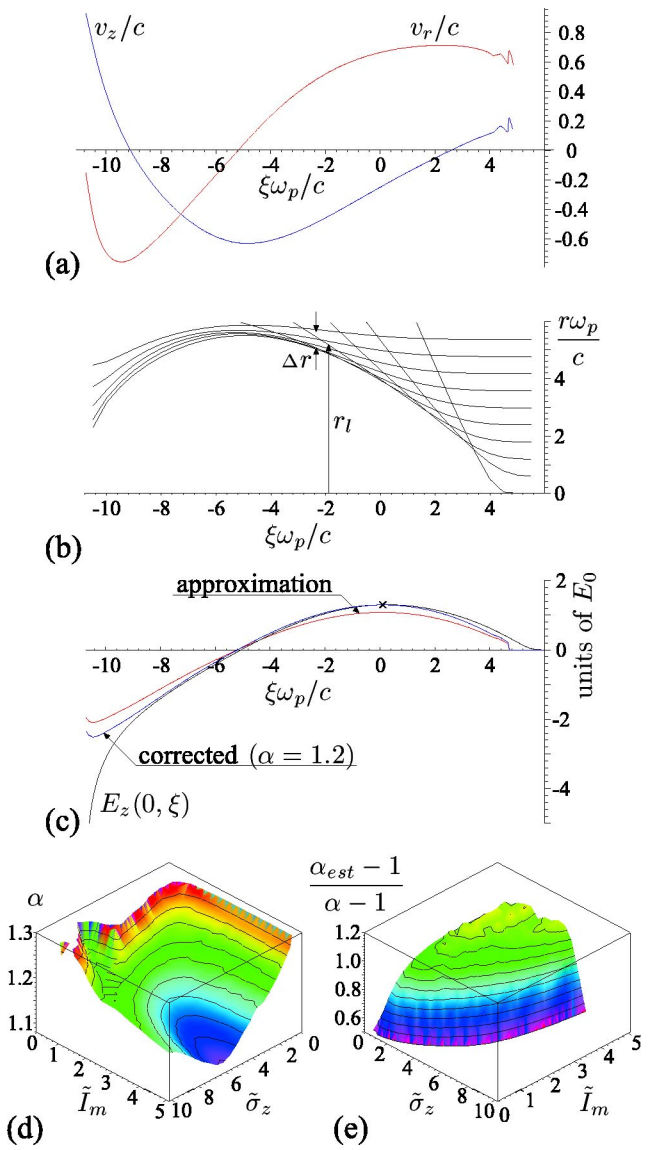

FIG. 3. (Color online) (a) Electron velocity in the screening layer (obtained by averaging over $n > 2n_0$ region), (b) trajectories of plasma electrons in the moving window (for estimation of Λ), (c) test of the estimate of Λ, (d) correction factor α, and (e) test of the estimate of α.

$$E_z(0,\xi) = \frac{4\pi e}{c}\int_0^\infty n v_r\, dr \approx \frac{4\pi e}{c}\Lambda v_r(r_l), \tag{15}$$

where r_l is the layer radius. To estimate Λ we notice that most of the plasma electrons flowing into the moving window in the circle of radius r_l gather in the screening layer of the thickness Δr [Fig. 3(b)]. The electron flux is steady in the moving window:

$$\pi r_l^2 n_0 c \approx 2\pi r_l \Delta r\, n(r_l)[c - v_z(r_l)], \tag{16}$$

from which

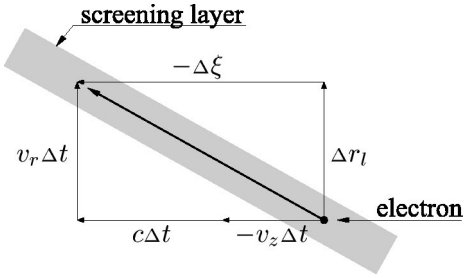

FIG. 4. Motion of the screening layer.

$$\Lambda \approx n(r_l)\Delta r \approx \frac{r_l n_0 c}{2(c-v_z)} \equiv \Lambda_{est} \tag{17}$$

(henceforth we omit the argument in designation of layer velocities). To check the precision of this nonrigorous estimate, in Fig. 3(c) we compare the exact value of the on-axis E_z with its approximation (15) and (17). In the wide interval of ξ, the estimate is correct up to 20%. Introduction of the correction factor $\alpha=1.20$ essentially improves the estimate. This factor may be explained by the fact that not only the $n>2n_0$ layer contributes to field creation. In what follows, we define α as the factor that makes the formula

$$E_z(0,\xi) \approx \frac{4\pi e\alpha}{c}\Lambda_{est} v_r = 2\pi n_0 e\alpha r_l \frac{v_r}{c-v_z} \tag{18}$$

strictly correct at the point of maximum positive E_z [marked by the cross in Fig. 3(c)]. In the strong beam region, α weakly depends on the beam current and linearly decreases as the beam length increases [Fig. 3(d)]:

$$\alpha \approx \alpha_{est} \equiv 1.29 - 0.033\ \sigma_z\omega_p/c; \tag{19}$$

the precision of this approximation is illustrated by Fig. 3(e).

With the expression for Λ, we can relate the shape of the cavern and the longitudinal field inside it. From simple geometrical considerations (Fig. 4) we have

$$\frac{dr_l}{d\xi} \approx -\frac{v_r}{c-v_z}, \tag{20}$$

whence

$$E_z(0,\xi) \approx -2\pi n_0 e\alpha r_l \frac{dr_l}{d\xi} = -\pi n_0 e\alpha \frac{dr_l^2}{d\xi}. \tag{21}$$

The precision of this approximation is illustrated by Fig. 5.

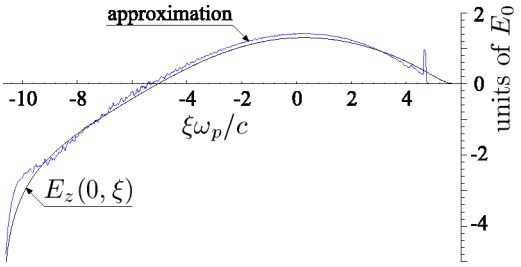

FIG. 5. (Color online) Relation between the cavern shape and the on-axis electric field.

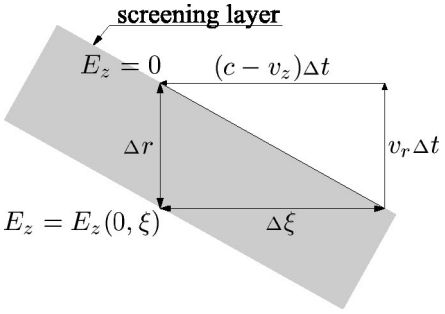

FIG. 6. Calculation of the field derivative in the layer.

As follows from Eqs. (11) and (12), the transverse fields in the cavern depend on the derivative $\partial E_z(0,\xi)/\partial\xi$. Let us relate this quantity to other cavern parameters. To this end, we integrate Eq. (7) and divide the integration interval into two parts as follows:

$$0 = \int_0^\infty \left(4\pi e(n+n_b-n_0) + \frac{\partial E_z}{\partial \xi}\right) r\, dr \approx \int_{\text{cavern}} + \int_{\text{layer}}. \tag{22}$$

Each part can be calculated or approximated:

$$\int_{\text{cavern}} = \frac{r_l^2}{2}\left(\frac{\partial E_z(0,\xi)}{\partial \xi} - 4\pi n_0 e\right) + \frac{2I_b(\xi)}{c}, \tag{23}$$

$$\int_{\text{layer}} \approx r_l \Delta r\left(\frac{\partial E_z(r_l,\xi)}{\partial \xi} + 4\pi e[n(r_l)-n_0]\right), \tag{24}$$

where $I_b(\xi)>0$ is the absolute value of the beam current. For the field derivative in the layer, we have (Fig. 6)

$$\frac{\partial E_z(r_l,\xi)}{\partial \xi} \sim -\frac{E_z(0,\xi)}{\Delta\xi} \sim -\frac{E_z(0,\xi)}{\Delta r}\frac{\Delta r}{\Delta\xi} \sim -\frac{E_z(0,\xi)}{\Delta r}\frac{v_r}{c-v_z}. \tag{25}$$

Inserting Eqs. (23)–(25) and (17) into Eq. (22), we find

$$\frac{\partial E_z(0,\xi)}{\partial \xi} \approx 4\pi n_0 e\left(1+\frac{2\Delta r}{r_l}\right) - \frac{4I_b(\xi)}{cr_l^2} + \frac{2v_r E_z(0,\xi)}{r_l(c-v_z)}$$
$$-\frac{8\pi e\Lambda}{r_l} \approx -\frac{4I_b(\xi)}{cr_l^2} - \frac{4\pi e n_0 v_z}{c-v_z} + \frac{2v_r E_z(0,\xi)}{r_l(c-v_z)}. \tag{26}$$

Denote the resultant three terms A_1, A_2, and A_3, respectively. These terms are plotted in Fig. 7 along with their sum and the field derivative itself. The approximation is seen to be quite good everywhere but the very beginning of the cavern.

As follows from Fig. 7, in the beam region (at the forepart of the cavern) the largest terms in Eq. (26) are the first (A_1) and the third (A_3) ones, while the field derivative is small. Physically, it means that the beam current is mainly compensated by the displacement current in the layer rather than by the layer current or displacement current in the cavern. Neglecting the smaller terms in Eq. (26), using Eq. (18), and omitting the correction factor α, we obtain

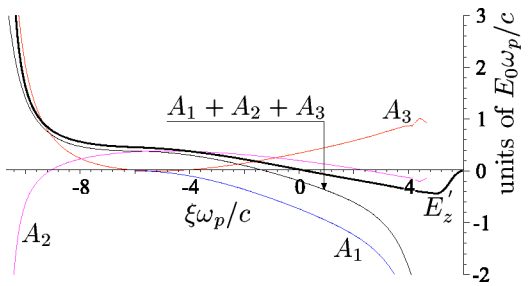

FIG. 7. (Color online) The field derivative E_z' and its approximations.

$$\frac{4I_b(\xi)}{cr_l^2} \approx \frac{2v_r E_z(0,\xi)}{r_l(c-v_z)} \approx \frac{E_z^2(0,\xi)}{\pi n_0 e r_l^2}. \tag{27}$$

This approximate equality gives us a remarkably simple estimate of the electric field in the first (beam) part of the cavern:

$$E_z(0,\xi) \approx \sqrt{\frac{4\pi n_0 e I_b(\xi)}{c}}, \quad \tilde{E}_z(0,\tilde{\xi}) \approx \sqrt{\tilde{I}_b(\tilde{\xi})}. \tag{28}$$

The check of this estimate is given in Fig. 8(a). Notice that the whole beam is predicted to fall into the region of decelerating field.

Now we can derive the shape of the diverging part of the cavern from Eq. (21),

$$r_l^2 \approx \int_{\xi}^{\infty} \sqrt{\frac{4I_b(\xi')}{\pi n_0 ec}}\, d\xi', \tag{29}$$

and estimate the maximum radius of the cavern for the Gaussian beam (2),

$$r_m^2 \approx 4\sigma_z \sqrt{\frac{I_{b,max}}{n_0 ec}}. \tag{30}$$

This maximum radius is reached approximately at the beam end. The field $E_z(0,\xi)$ changes its sign also here. The predicted cavern shape for the cosine beam (1) is shown in Fig. 8(b) (right curve).

Let us obtain the law of motion for the screening layer at the converging part of the cavern [where $I_b(\xi)=0$]. We assume that the motion is determined by fields at the layer inner boundary:

$$E_z \approx E_z(0,\xi) \approx \frac{2\pi n_0 e \alpha r_l v_r}{c-v_z}, \tag{31}$$

$$\begin{aligned} B_\varphi &\approx -\frac{r_l}{2}\frac{\partial E_z(0,\xi)}{\partial \xi} \\ &\approx \frac{2\pi n_0 e r_l v_z}{c-v_z} - \frac{v_r E_z(0,\xi)}{c-v_z} \\ &\approx 2\pi n_0 e r_l \left(\frac{v_z}{c-v_z} - \frac{\alpha v_r^2}{(c-v_z)^2}\right), \end{aligned} \tag{32}$$

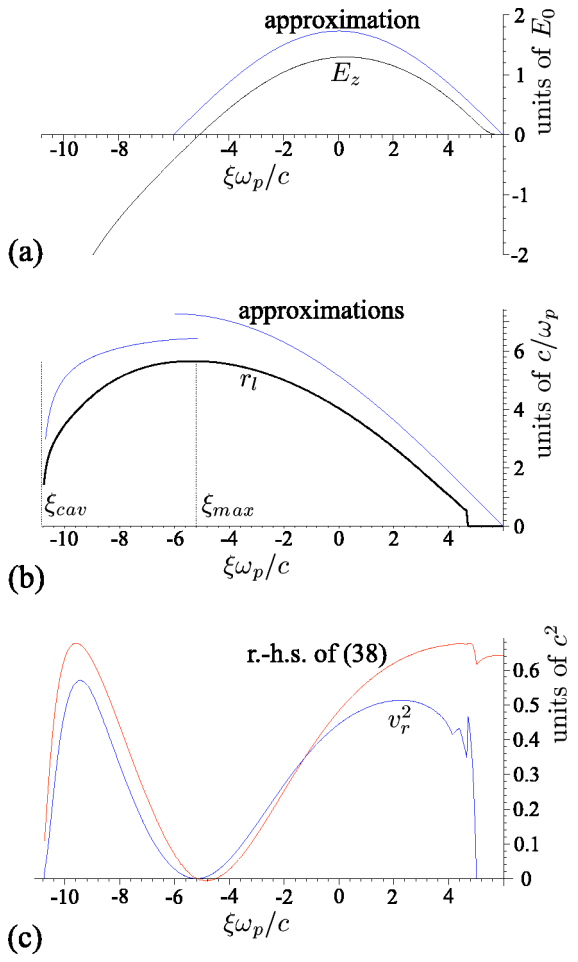

FIG. 8. (Color online) Simulation results and analytical approximations for the longitudinal electric field (a), cavern radius (b), and radial layer velocity (c).

$$E_r \approx 2\pi n_0 e r_l - \frac{r_l}{2}\frac{\partial E_z(0,\xi)}{\partial \xi} \approx 2\pi n_0 e r_l \left(\frac{c}{c-v_z} - \frac{\alpha v_r^2}{(c-v_z)^2}\right) \tag{33}$$

[we have used Eqs. (12), (18), and (26) here]. The law of electron motion (3) in terms of velocities reads as

$$\frac{dv_r}{d\xi} = \frac{e}{\gamma m(c-v_z)}\left[\left(1-\frac{v_r^2}{c^2}\right)E_r - \frac{v_r v_z}{c^2}E_z - \frac{v_z}{c}B_\varphi\right],$$

$$\frac{dv_z}{d\xi} = \frac{e}{\gamma m(c-v_z)}\left[\left(1-\frac{v_z^2}{c^2}\right)E_z - \frac{v_r v_z}{c^2}E_r + \frac{v_r}{c}B_\varphi\right],$$

where γ is the relativistic factor of electrons. Substituting the fields (31)–(33) into this law yields

$$\frac{dv_r}{d\xi} \approx \frac{\omega_p^2 r_l}{2\gamma^3 c\,(1-v_z/c)^2}\left(1-\frac{\alpha v_r^2/c^2}{1-v_z/c}\right), \tag{34}$$

$$\frac{dv_z}{d\xi} \approx \frac{\omega_p^2 r_l}{2\gamma^3 c\,(1-v_z/c)^2}\frac{\alpha v_r}{c} \tag{35}$$

and forms, together with Eq. (20), a closed set of equations.

We can relate the velocity components dividing Eq. (34) by Eq. (35):

$$\frac{du_r}{du_z} \approx \frac{\alpha u_r^2/u_z - 1}{\alpha u_r}, \quad u_r = v_r/c, \quad u_z = 1 - v_z/c. \tag{36}$$

The solution to this equation is

$$\alpha u_r^2 = 2u_z\left(1 - \frac{u_z}{u_0}\right), \quad u_0 = \text{const}, \tag{37}$$

or, in the dimensional form,

$$v_r^2 \approx \frac{2(c-v_z)}{\alpha}\left(c - \frac{c-v_z}{1-v_{z,max}/c}\right), \tag{38}$$

where $v_{z,max}$ is the layer velocity at the widest part of the cavern (where $v_r=0$). The test of Eq. (38) is shown in Fig. 8(c).

Dividing Eq. (35) by Eq. (20) and excluding v_r, we obtain

$$\frac{du_z}{d\tilde{r}_l} \approx \frac{\alpha \tilde{r}_l}{2\gamma^3 u_z}, \tag{39}$$

where

$$\frac{1}{\gamma^2} = 1 - \frac{v_r^2}{c^2} - \frac{v_z^2}{c^2} \approx \frac{u_z[\alpha u_0(2-u_z) + 2(u_z-u_0)]}{\alpha u_0}, \tag{40}$$

$$\tilde{r}_l = \frac{\omega_p r_l}{c}, \quad u_0 = 1 - v_{z,max}/c. \tag{41}$$

Equation (39) has the analytical solution

$$\tilde{r}_l^2 \approx \frac{4\sqrt{\alpha u_0 u_z}}{(\alpha-1)\sqrt{\alpha u_0(2-u_z) + 2(u_z-u_0)}}, \tag{42}$$

the test of which is shown in Fig. 8(b) (left curve). The maximum cavern radius is thus related to the layer velocity at this place:

$$\tilde{r}_m^2 \approx \frac{4}{\alpha-1}\sqrt{\frac{u_0}{2-u_0}}, \tag{43}$$

or, in the dimensional form,

$$r_m \approx \frac{2c}{\omega_p\sqrt{\alpha-1}}\left(\frac{c-v_{z,max}}{c+v_{z,max}}\right)^{1/4}. \tag{44}$$

Notice that, due to the factor $\sqrt{\alpha-1}$ in denominators, approximations (42)–(44) are very sensitive to the choice of α.

Substituting Eqs. (37) and (42) into the dimensionless form of Eq. (20),

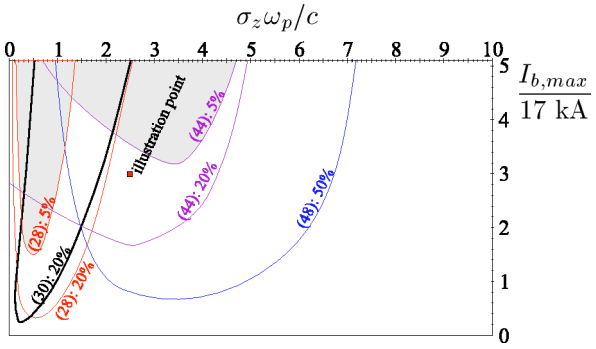

FIG. 9. (Color online) Map of precision for several analytic estimates. The numbers in parentheses refer to the equations in the text.

$$\frac{d\tilde{r}_l^2}{d\tilde{\xi}} \approx -\frac{2\tilde{r}_l u_r}{u_z}, \tag{45}$$

we obtain the equation for determination of v_z as a function of ξ:

$$\frac{du_z}{d\tilde{\xi}} \approx \frac{u_z^{1/4}[\alpha u_0(2-u_z) + 2(u_z-u_0)]^{5/4}\sqrt{2(u_0-u_z)}}{\alpha^{3/4}u_0^{7/4}\sqrt{\alpha-1}} \equiv U(u_z,u_0). \tag{46}$$

This equation has no solutions in elementary functions except for the whole integration interval from the cavern end (at ξ_{cav}) to the widest place (at ξ_{max}):

$$\frac{(\xi_{max}-\xi_{cav})\omega_p}{c} \approx \int_0^{u_0}\frac{du_z}{U(u_z,u_0)} = \frac{\sqrt{2}\,[\Gamma(0.75)]^2}{\sqrt{\pi}}\left(\frac{u_0}{2-u_0}\right)^{3/4} \approx 1.2\left(\frac{c-v_{z,max}}{c+v_{z,max}}\right)^{3/4}, \tag{47}$$

where Γ is the Gamma function. Using Eqs. (44), (30), and (19), we obtain

$$\tilde{\xi}_{max} - \tilde{\xi}_{cav} \approx (4\times10^{-3})\,\tilde{I}_m^{3/4}\,\tilde{\sigma}_z^{3/2}(39-\tilde{\sigma}_z)^{3/4}(8.8-\tilde{\sigma}_z)^{3/2}. \tag{48}$$

In our illustrative case, this formula predicts the value of 7.8 c/ω_p for the length of the converging part, while the simulation gives 6.2 c/ω_p.

The above illustrations show the precision of the analytical estimates for one special case only. The general map of precision for key formulas is shown Fig. 9. It is seen that the above estimates are correct in a wide region of parameters. Surprisingly, the estimate (28) for the peak decelerating field turns out to be very accurate between the strong beam and short beam areas.

There is an interesting observation which can be explained by the above theory; namely, in the strong beam regime, E_z decreases almost linearly in a wide interval of ξ [dotted line in Fig. 2(g)]:

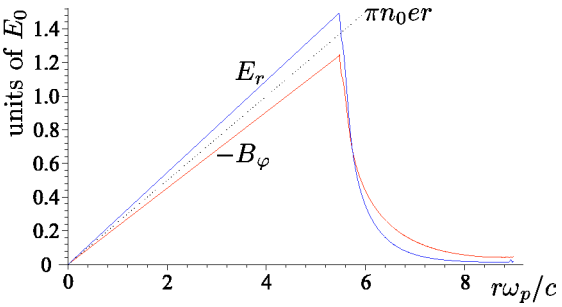

FIG. 10. (Color online) Radial field profiles behind the beam ($\xi\omega_p/c=6$).

$$\frac{\partial E_z(0,\xi)}{\partial \xi} \approx 2\pi n_0 e. \tag{49}$$

This contrasts with one-dimensional strongly nonlinear wakefields for which this derivative is twice greater (see, e.g., Ref. [32]). Formula (49) follows from Eq. (26) and Fig. 7. Around the widest part of the cavern, the main contribution to the field derivative comes from the second term A_2, which approaches $2\pi n_0 e$ as the layer velocity tends to the relativistic limit ($v_z \to -c$). The constant field derivative (49) makes the right-hand sides of Eqs. (11) and (12) nearly equal in absolute values, and we have

$$E_r \approx -B_\varphi \approx \pi n_0 e r \tag{50}$$

just behind the beam (Fig. 10).

V. SCALINGS FOR GEOMETRICAL PARAMETERS OF THE CAVERN

The best place for location of accelerated particles in the blowout PWFA is near the cavern end, where the accelerating field is the highest. Shortening of the cavern caused, e.g., by the driver depletion or a plasma density variation, may be fatal for accelerated particles if they fall into the defocusing region of the wakefield. Therefore it is important to realize scalings of cavern geometrical parameters. The main parameters are the maximum radius r_m, location of the field zero (ξ_{max}), location of the field singularity (ξ_{cav}), and closing angle of the cavern (α_c) (Fig. 11).

The behavior of the cavern radius is shown in Fig. 12(a). The radius monotonically increases with the beam current. As a function of the beam length, the radius has a maximum in the strong beam region and slowly decreases toward the

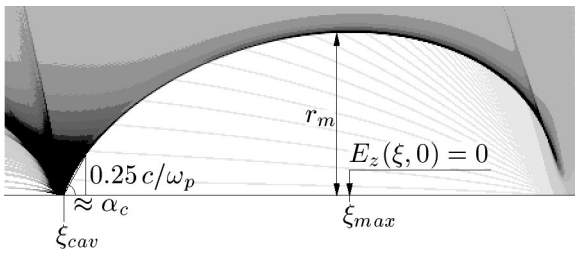

FIG. 11. Geometrical parameters of the cavern and the method of approximation of α_c.

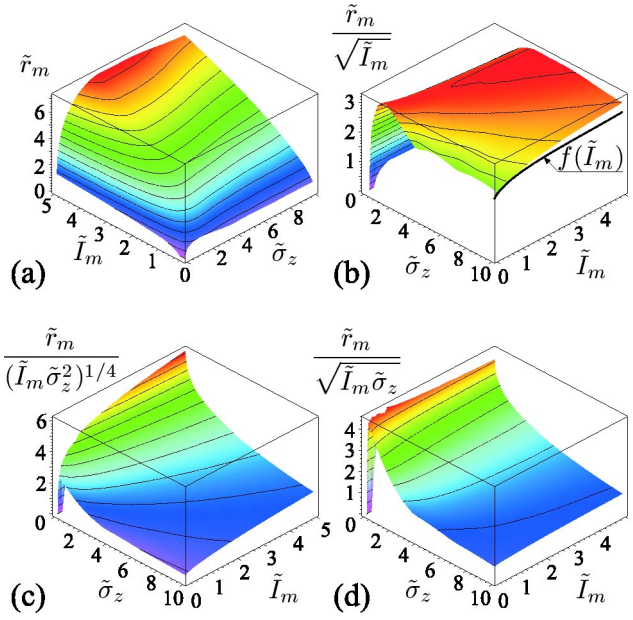

FIG. 12. (Color online) Radius of the cavern (a) and its scalings in ion channel (b), strong beam (c), and short beam (d) regimes.

ion channel value while the beam length increases. In the main blowout regimes, we have the following approximations for the cavern radius:

$$\text{ion channel: } \tilde{r}_m \approx \sqrt{\tilde{I}_m}\, f(\tilde{I}_m), \quad f(\tilde{I}_m) \in (2, 2\sqrt{2}); \tag{51}$$

$$\text{strong beam: } \tilde{r}_m \approx 3.8\, \tilde{I}_m^{1/4} \tilde{\sigma}_z^{1/2}; \tag{52}$$

$$\text{short beam: } \tilde{r}_m \approx 4.2\sqrt{\tilde{I}_m \tilde{\sigma}_z}; \tag{53}$$

the accuracy of which is illustrated by Fig. 12(b)–12(d). Formula (51) follows from the ion channel theory [26], expression (52) is the dimensionless form of Eq. (30); and Eq. (53) is obtained empirically. Note that, although the surfaces in Fig. 12(c) and 12(d) have no plateau, they cross the asymptotic values at correct places, which means an agreement with the approximate formulas.

The location of the zero-field cross section is shown in Fig. 13(a). For short beams, the length of the decelerating field region (limited by ξ_{max}) linearly increases with the beam current:

$$|\tilde{\xi}_{max}| \approx 1.95 + 0.6\, \tilde{I}_m. \tag{54}$$

For strong beams, the theory predicts that ξ_{max} is located near the beam end and its absolute value grows proportionally to σ_z. The thick line in Fig. 13(a) marks the place where $\xi_{max} = -2.5\,\sigma_z$. For the ion channel regime, the field changes its sign near the beam center, and we observe the decrease of $|\xi_{max}|$, as the beam length increases. At low currents, the oscillating component of the longitudinal field affects the location of the zero-field point and somewhat shifts it forward or backward relatively to the beam center.

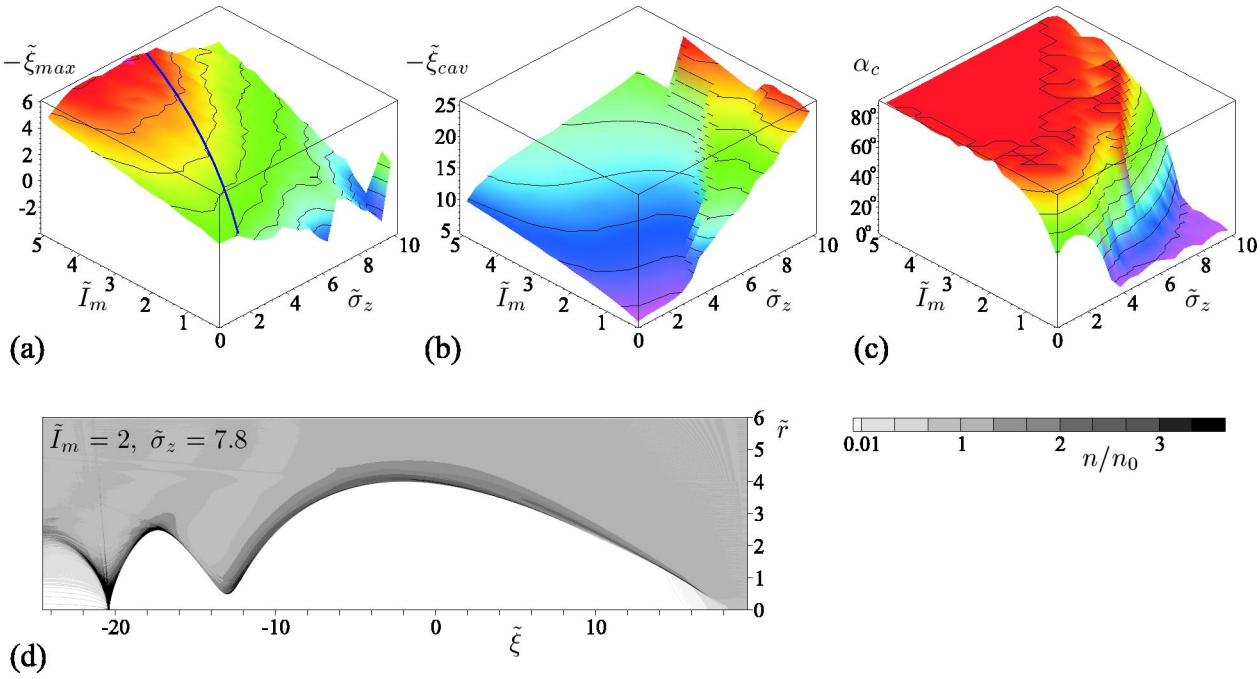

FIG. 13. (Color online) Location of the zero-field point (a), location of the field singularity (b), and closing angle (c) as functions of beam length and current; illustration of merging of the first and second caverns (d).

The location of the field singularity is shown in Fig. 13(b). We do not find simple scalings for this quantity. Near the boundary of the ion channel region we observe an abrupt change of ξ_{cav} caused by merging of the first and the second caverns [Fig. 13(d)].

The closing angle is shown in Fig. 13(c). It is close to 90° for high beam currents and moderately long beams. This is favorable for wakefield acceleration, since the region of the good field is wide. In the ion channel regime, the cavern ends gently ($\alpha_c \to 0$). The experimentally investigated area of E-157 experiment falls into the transition region between the two extreme cases.

The closing angle also shows the velocity of plasma electrons near the end of the cavern, since

$$\tan \alpha_c = \frac{v_r}{v_z - c}. \tag{55}$$

The right closing angle means that the electrons move along the beam axis with relativistic velocity $v_z \approx c$. Zero closing angle indicates that the electron motion is not relativistic. Intermediate angles are possible only for a relativistic motion with $v_r \sim v_z \sim c$.

It is instructive to look at the motion of plasma electrons in the laboratory frame of reference (Fig. 14). In the ion channel regime [Fig. 14(a)], the electrons move backward and remain at the shifted positions. Strong and short beam regimes have no qualitative differences [Figs. 14(b) and 14(c)]: near-axis electrons are scattered away, mainly in the radial direction, while most of perturbed electrons make a circle near their initial position. Some of electrons are even entrained by the beam and move forward.

VI. ENERGY FLUX

In the presence of the beam, there appears an energy flow along the comoving window. This flow is composed by the energy flow in the laboratory frame and the energy transfer

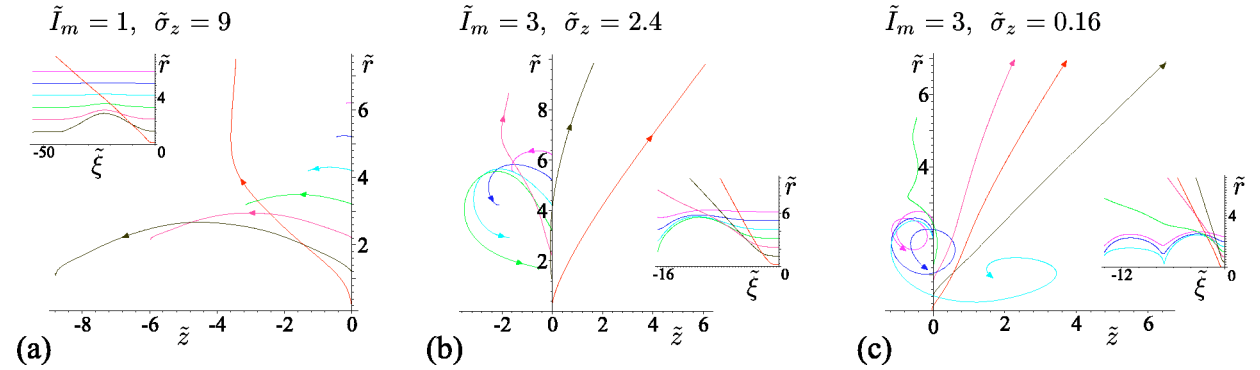

FIG. 14. (Color online) Motion of plasma electrons in the laboratory frame for ion channel (a), strong beam (b), and short beam (c) regimes. Insets show trajectories of the same electrons in the moving window.

due to motion of the window. Denoting the unit vector in the beam direction by $\vec{e}_z$, we can write the flux density of the electromagnetic energy as

$$\vec{S}_{em} = -c\,\vec{e}_z \frac{E^2+B^2}{8\pi} + \frac{c}{4\pi}[\vec{E}\times\vec{B}] \tag{56}$$

and the total energy flux density in the comoving window as

$$\vec{S} = \vec{S}_{em} + \sum (\gamma - 1)mc^2(\vec{v} - c\,\vec{e}_z), \tag{57}$$

where the summation is carried out over plasma particles in the unit volume. For zero-temperature fluid plasma models, the energy flux density is

$$\vec{S}_f = \vec{S}_{em} + nmc^2(\gamma - 1)(\vec{v} - c\,\vec{e}_z). \tag{58}$$

Integrating Eqs. (56)–(58) yields us the energy fluxes along the window, for example,

$$\Psi = -\int_0^\infty S_z\, 2\pi r\, dr, \quad \Psi_f = -\int_0^\infty S_{fz}\, 2\pi r\, dr. \tag{59}$$

It is easy to check straightforward that the total energy flux is the measure of beam-plasma energy exchange:

$$\frac{\partial \Psi}{\partial \xi} = \int_0^\infty j_{bz} E_z\, 2\pi r\, dr, \quad j_{bz} = -en_b c. \tag{60}$$

The difference between Ψ and Ψ_f can serve as a measure of the lost energy which cannot be retrieved by the accelerated beam. In the absence of beams and nearby walls, the derivative $\partial\Psi/\partial\xi$ must be zero; this can be used as a good test of precision for simulation codes.

For low-density beams and a linearly respondent plasma, the expression for the flux density can be written analytically in the most interesting cases. To this end, we use the textbook formula [2] for the longitudinal wakefield:

$$E_z(r,\xi) = 4\pi e k_p^2 \int_\infty^\xi d\xi' \int_0^\infty \cos\, k_p(\xi - \xi') I_0(k_p r_<) \times K_0(k_p r_>) n_b(r', \xi') r'\, dr', \tag{61}$$

where

$$k_p = \omega_p/c, \quad r_< = \min(r, r'), \quad r_> = \max(r, r'), \tag{62}$$

and I_0 and K_0 are the modified Bessel functions of zero order. If the beam density is factorable, i.e.,

$$n_b(r,\xi) = n_{bm} R_{nb}(r) Z_{nb}(\xi), \tag{63}$$

then the field behind the beam has the form

$$E_z = E_{zm} \cos(k_p \xi + \varphi_0) R_{ez}(r), \tag{64}$$

$$R_{ez}(r) = k_p^2 \int_0^\infty I_0(k_p r_<) K_0(k_p r_>) R_{nb}(r) r'\, dr'. \tag{65}$$

For the Gaussian beam (2), we have

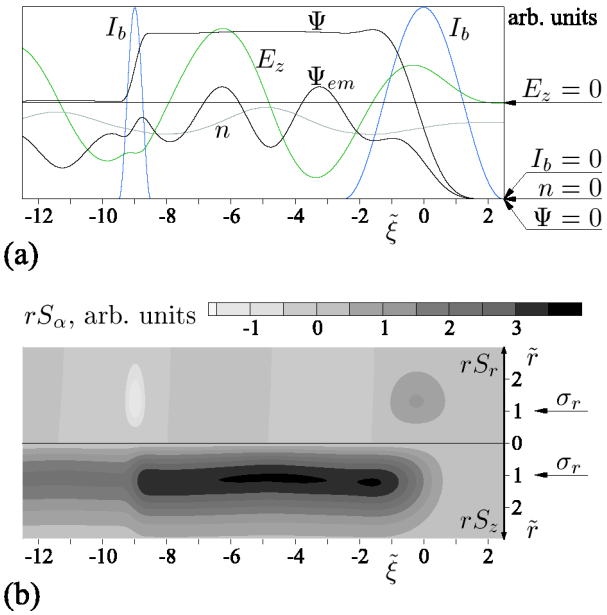

FIG. 15. (Color online) Example of a weakly nonlinear wakefield: (a) the beam current I_b, excited wakefield E_z, electron density n, and energy fluxes Ψ and Ψ_{em}; (b) spatial distribution of the energy flux density.

$$E_{zm} = E_0 \frac{2\sqrt{2\pi}\tilde{\sigma}_z \tilde{I}_m}{\tilde{\sigma}_r^2} e^{-\tilde{\sigma}_z^2/2}, \quad \varphi_0 = \pi. \tag{66}$$

In the case of linear plasma response, the longitudinal velocity of the electron fluid v_z plays the role of the wakefield potential and no magnetic field is left behind the beam:

$$\tilde{E}_z = \frac{\partial \tilde{v}_z}{\partial \tilde{\xi}}, \quad \tilde{E}_r = \frac{\partial \tilde{v}_z}{\partial \tilde{r}} = \frac{\partial \tilde{v}_r}{\partial \tilde{\xi}}, \quad \tilde{B}_\varphi = 0, \tag{67}$$

whence, in the highest term, we obtain the energy flux density behind the factorable beam (63):

$$-\tilde{S}_z \equiv -\frac{S_z}{n_0 mc^3} = \frac{\tilde{E}_z^2 + \tilde{E}_r^2}{2} + \frac{\tilde{v}_r^2 + \tilde{v}_z^2}{2} = \frac{\tilde{E}_{zm}^2}{2}\left[R_{ez}^2 + \left(\frac{\partial R_{ez}}{\partial \tilde{r}}\right)^2\right]. \tag{68}$$

It does not depend on ξ and is directly related to the amplitude and radial distribution of E_z.

The behavior of the energy flux for a low-density beam is illustrated by Fig. 15, where the second beam is accelerated by the wakefield of the first beam. The flux density S_z is maximal on the axis, though most part of the energy is transmitted at radii of the order of σ_r or c/ω_p, whatever is greater. Note that the electromagnetic energy flux [Fig. 15(a)] oscillates around half of the total flux, as it should be in linear Langmuir waves.

Figure 15(b) also shows how a weak plasma nonlinearity changes the above idealized picture. As the on-axis electron density increases, the energy flow shifts toward the axis, and vice versa. Small oscillations of Ψ between the beams are a numerical artifact; this is the way how the finite radius of the simulation window can disturb the energy balance (for the twice wider simulation window, the oscillations become invisible).

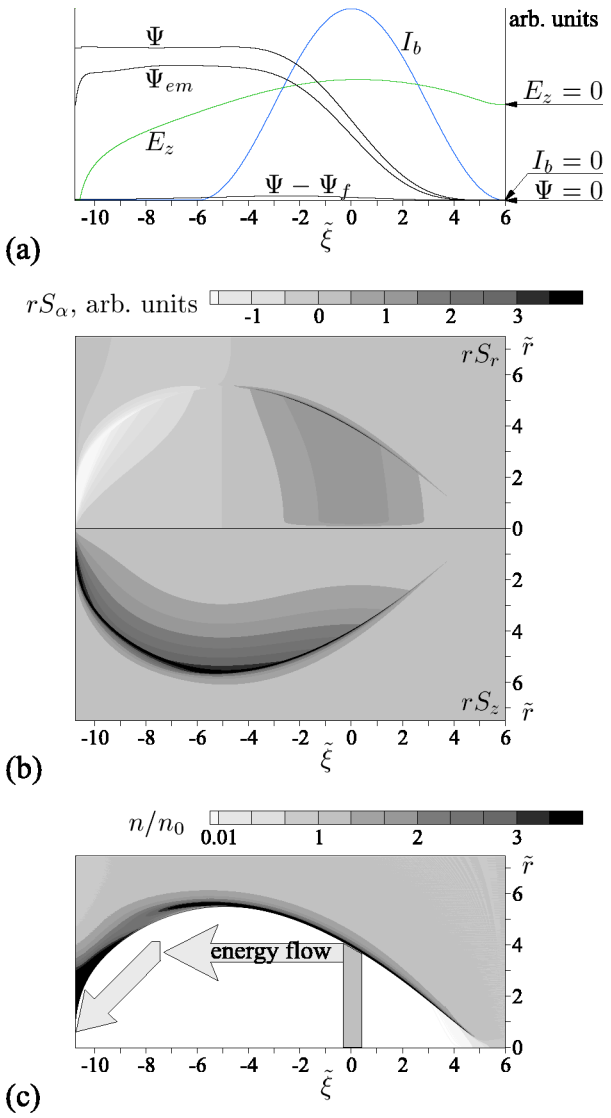

FIG. 16. (Color online) Energy flow in the strong beam regime [the same beam as in Fig. 2(g)]: (a) the beam current I_b, excited wakefield E_z, and the energy fluxes (total Ψ, electromagnetic Ψ_{em}, and thermal $\Psi-\Psi_f$), (b) spatial distribution of the energy flux density, and (c) directions of the energy flow on the density map.

A typical behavior of the energy flux in the blowout regime is shown in Fig. 16. A major part of the energy is transmitted via the electromagnetic field [Fig. 16(a)]. There appears a small difference between Ψ and Ψ_f, which means that some energy is irretrievably lost with scattered near-axis electrons. The map of the energy flux density [Fig. 16(b)] shows that the cavern boundary acts as a "mirror" that focuses the energy to the singularity point at the end of the cavern [Fig. 16(c)].

The dependence of the dimensionless energy flux

$$\tilde{\Psi} = \Psi \frac{4\pi e^2}{m^2 c^5} \tag{69}$$

on the beam parameters is shown in Fig. 17 for two cross sections. Given a peak current, the most efficient energy

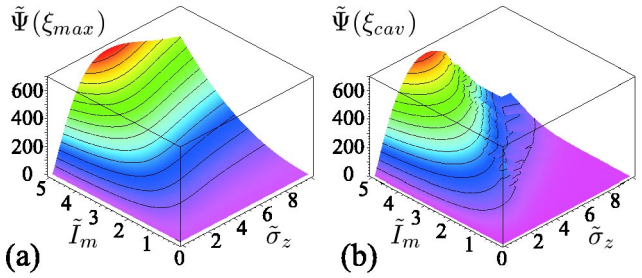

FIG. 17. (Color online) Total energy flux at the zero-field cross-section (a) and at the cavern end (b).

transfer occurs in the strong beam regime. The maximum of $\tilde{\Psi}$ is exactly at the beam length for which the cavern width is maximal [Fig. 2(a)]. For a fixed beam charge, the maximum energy is transferred to plasma at $\sigma_z \approx 0.6\, c/\omega_p$ independent of the beam current. The difference between Figs 17(a) and 17(b) shows the energy taken back by the tail of a long beam.

Let us write out approximate formulas for the energy flux behind the beam in two blowout regimes. In the strong beam regime, it is convenient to calculate the total flux at the widest place of the cavern, where $E_z=0$ on the axis. For the total electromagnetic flux, we use Eqs. (56) and (50) to obtain

$$\begin{aligned}\Psi_{em} &\approx \frac{c}{8\pi}\int_0^\infty (E_r - B_\varphi)^2\, 2\pi r\, dr \\ &\approx \frac{c}{4}\int_0^{r_m} (2\pi n_0 e r)^2\, r\, dr \\ &= \frac{\pi^2 e^2 n_0^2 c}{4} r_m^4. \end{aligned} \tag{70}$$

The contribution of plasma kinetic energy to the energy flux is made mainly by the screening layer. It can be approximated as

$$\begin{aligned}\Psi_{\text{layer}} &\approx \int_{\text{layer}} nmc^2(\gamma-1)(c-v_z)\, 2\pi r\, dr \\ &\approx mc^2 \Lambda(\gamma-1)(c-v_z) 2\pi r_m \\ &\approx \frac{2\pi n_0 mc^5}{\omega_p^2(\alpha-1)}\left(\frac{\tilde{r}_m^2(\alpha-1)}{4}-1\right)^2, \end{aligned} \tag{71}$$

where we use Eqs. (58), (17), and the consequence of Eq. (44):

$$\gamma - 1 \approx \frac{1}{\sqrt{1-v_z^2/c^2}} - 1 \approx \frac{2}{\tilde{r}_m^2(\alpha-1)}\left(\frac{\tilde{r}_m^2(\alpha-1)}{4}-1\right)^2. \tag{72}$$

The total energy flux in the dimensionless form is

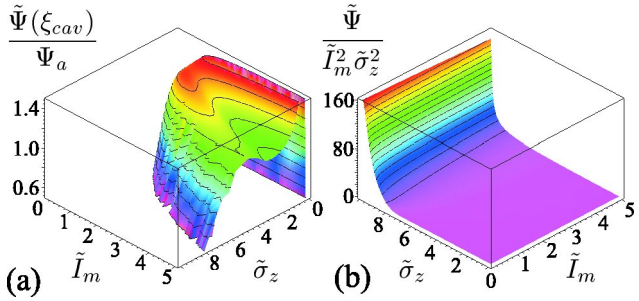

FIG. 18. (Color online) Precision of the estimates of the total energy flux for strong (a) and short (b) beams.

$$\tilde{\Psi} = \tilde{\Psi}_{em} + \tilde{\Psi}_{\text{layer}} \approx \frac{\pi \tilde{r}_m^4}{16} + \frac{2\pi}{\alpha - 1}\left(\frac{\tilde{r}_m^2(\alpha - 1)}{4} - 1\right)^2 \equiv \Psi_a. \tag{73}$$

The precision of this estimate [with the expression (19) for α] is illustrated by Fig. 18(a). Insertion of Eq. (30) into Eq. (73) does not result in a satisfactory estimate of Ψ since the error of r_m raised to the fourth power is too large.

For the short beam regime, the energy flux can be found in terms of the instant push. An electron located close to the beam at some radius r gets the transverse momentum

$$\Delta p_\perp \approx \frac{2eQ}{r}, \quad Q = \frac{\sqrt{2\pi} I_{b,max} \sigma_z}{c}, \tag{74}$$

where Q is the total beam charge. The energy lost by the beam per unit path length can be estimated as

$$\frac{\Psi}{c} \approx n_0 \int_{\sigma_r}^{c/\omega_p} \frac{\Delta p_\perp^2}{2m} 2\pi r \, dr \approx \frac{4\pi n_0 e^2 Q^2}{m} \ln \frac{c/\omega_p}{\sigma_r} \tag{75}$$

or

$$\tilde{\Psi} \approx (\tilde{I}_m \tilde{\sigma}_z)^2 8\pi^2 \Lambda_c, \quad \Lambda_c \equiv -\ln \tilde{\sigma}_r. \tag{76}$$

For the illustrating case of $\tilde{\sigma}_r = 0.1$, we have

$$\Lambda_c \approx 2, \quad \tilde{\Psi} \approx 160(\tilde{I}_m \tilde{\sigma}_z)^2 \tag{77}$$

in good agreement with numerical observations [Fig. 18(b)].

VII. SUMMARY

We numerically scanned a wide region of beam parameters and clarified the dependence of main cavern properties on the beam length and current for the blowout type of beam-plasma interaction. Three main regimes of the plasma response were found, which qualitatively differs in the plasma behavior. These regimes are the ion channel regime which can be described analytically by the infinite beam model [25–28], the strong beam regime which allows us to make analytical approximations correct up to tens of per cent, and the short beam regime which can be understood in terms of interaction of a point charge with the plasma.

To characterize the efficiency of the beam-plasma energy exchange, we introduced the energy flux density and the total energy flux in the comoving window. We studied scalings of the total energy flux for linear and blowout plasma responses and revealed that the most efficient energy transfer occurs in the strong beam regime of interaction. Operation in the strong beam regime requires high beam currents (tens of kiloamperes) that are not available at today's experimental facilities, but achievable in future experiments by a longitudinal compression of a high-energy beam.

ACKNOWLEDGMENTS

This work was supported by Science Support Foundation, SB RAS Lavrent'ev Grant for young researchers, Russian Foundation for Basic Research (Grant No. 03-02-16160a), and Russian Ministry of Science (Grant No. NSh-229.2003.2).

[1] P. Chen, J. M. Dawson, R. W. Huff, and T. Katsouleas, Phys. Rev. Lett. **54**, 693 (1985); **55**, 1537(E) (1985).
[2] E. Esarey, P. Sprangle, J. Krall, and A. Ting, IEEE Trans. Plasma Sci. **24**, 252 (1996).
[3] C. Joshi *et al.*, Phys. Plasmas **9**, 1845 (2002).
[4] R. W. Assmann, in Proceedings of the Eighth European Particle Accelerator Conference, Paris, 2002 (unpublished), p. 64.
[5] P. Chen *et al.*, Phys. Rev. Lett. **56**, 1252 (1986).
[6] R. D. Ruth, A. W. Chao, P. L. Morton, and P. B. Wilson, Part. Accel. **17**, 171 (1985).
[7] K. V. Lotov, Nucl. Instrum. Methods Phys. Res. A **410**, 461 (1998).
[8] J. B. Rosenzweig, B. Breizman, T. Katsouleas, and J. J. Su, Phys. Rev. A **44**, R6189 (1991).
[9] N. Barov and J. B. Rosenzweig, Phys. Rev. E **49**, 4407 (1994).
[10] J. Krall and G. Joyce, Phys. Plasmas **2**, 1326 (1995).
[11] S. Lee, T. Katsouleas, R. Hemkel, and W. Mori, Phys. Rev. E **61**, 7014 (2000).
[12] E. S. Dodd *et al.*, Phys. Rev. Lett. **88**, 125001 (2002).
[13] R. Hemkel, W. Mori, S. Lee, and T. Katsouleas, Phys. Rev. ST Accel. Beams **3**, 061301 (2000).
[14] D. L. Bruhwiler *et al.*, Phys. Rev. ST Accel. Beams **4**, 101302 (2001).
[15] K. V. Lotov, Phys. Rev. ST Accel. Beams **6**, 061301 (2003).
[16] J. B. Rozenzweig *et al.*, Phys. Rev. Lett. **61**, 98 (1988).
[17] J. B. Rozenzweig *et al.*, Phys. Rev. A **39**, 1586 (1989).
[18] N. Barov, M. E. Conde, W. Gai, and J. B. Rosenzweig, Phys. Rev. Lett. **80**, 81 (1998).
[19] N. Barov *et al.*, Phys. Rev. ST Accel. Beams **3**, 011301 (2000).
[20] M. J. Hogan *et al.*, Phys. Plasmas **7**, 2241 (2000).
[21] C. E. Clayton *et al.*, Phys. Rev. Lett. **88**, 154801 (2002).
[22] S. Wang *et al.*, Phys. Rev. Lett. **88**, 135004 (2002).
[23] LCODE is available free at www.inp.nsk.su/~lotov/lcode
[24] P. Mora and T. M. Antonsen, Phys. Plasmas **4**, 217 (1997).
[25] D. H. Whittum, Phys. Fluids B **4**, 476 (1992).

[26] K. V. Lotov, Phys. Plasmas **3**, 2753 (1996).
[27] I. A. Kotelnikov and V. N. Khudik, Plasma Phys. Rep. **23**, 130 (1997).
[28] V. N. Khudik and K. V. Lotov, Plasma Phys. Rep. **25**, 149 (1999).
[29] D. H. Whittum *et al.*, Phys. Rev. Lett. **67**, 991 (1991).
[30] M. Lampe, G. Joyce, S. P. Slinker, and D. H. Whittum, Phys. Fluids B **5**, 1888 (1993).
[31] A. A. Geraci and D. H. Whittum, Phys. Plasmas **7**, 3431 (2000).
[32] J. B. Rosenzweig, Phys. Rev. Lett. **58**, 555 (1987).